Journal of Applied Fluid Mechanics, Vol. 17, No. 12, pp. 2708-2719, 2024.
Available online at www.jafmonline.net, ISSN 1735-3572, EISSN 1735-3645.
https://doi.org/10.47176/jafm.17.12.2690

Experimental Investigation of Aerodynamic Noise Characteristics of Tandem Asymmetric Airfoils Across Varied Angles of Attack

W. Shi [1], Y. Li[1], J. Zhou[1†] and Z. Chen [2]

[1] *College of Mechanical and Electrical Engineering, Wenzhou University, Wenzhou, Zhejiang 325035 China*
[2] *Key Laboratory of Aerodynamic Noise Control, China Aerodynamics Research and Development Center, Mianyang, Sichuan, 621000, China*

†Corresponding Author Email: zhoujxi@wzu.edu.cn

ABSTRACT

This paper experimentally investigates the aerodynamic noise characteristics of a tandem asymmetric airfoil-airfoil at different angles of attack in the 0.5 m×0.4 m acoustic wind tunnel at Wenzhou University. Based on the airfoil chord length and the wind speed, the Reynolds number ranges between 2.2×10^5 and 3.5×10^5. Meanwhile, the attack angle (α_1 and α_2) of both tandem airfoils varies between 0~20°, and the noise is measured using a far/near-field microphone array. The experimental results indicate that when the attack angle α_1 of the upstream airfoil is small (α_1<15°), its wake hardly interacts with the downstream airfoil, and the noise source is mainly concentrated at the trailing edge of the upstream airfoil. When the attack angle α_1 is larger than 15°, the upstream wake interacts with the downstream airfoil, the noise radiates from the leading edge of the downstream airfoil, and the source location varies slightly at different frequencies. Compared to the upstream attack angle α_1, the downstream airfoil attack angle α_2 has less impact on the aerodynamic noise of the tandem airfoils. Additionally, the particle imaging velocimetry technique is employed to measure the flow field characteristics and analyze the mechanism of noise production.

Article History

Received February 28, 2024
Revised May 12, 2024
Accepted June 1, 2024
Available online October 2, 2024

Keywords:

Aerodynamic noise
Angles of attack
Tandem asymmetric airfoil
Tone noise
Turbulence-surface interaction

1. INTRODUCTION

Axial fans have been widely used in petrochemical, mining, aerospace, transportation, electronic machinery, and household equipment for heat dissipation and air ventilation. However, the unsteady flow caused by axial flow fans leads to noise issues that are difficult to solve. Longhouse (1976) classified the broadband noise of axial flow fans into non-rotating noise and the tonal noise into rotating noise. One of the main sources of tonal noise is the interaction between the trailing flow of the upstream rotor and the downstream stators, where the shedding vortex generated by the trailing edge of the upstream rotor interacts with the downstream stators. This type of noise is unavoidable and only can be reduced. Tandem airfoils can be considered as a simple model of rotor and stator in axial fans, so the focus of this paper is to investigate the noise characteristics and variations of the tandem airfoil at different angles of attack.

Vortex-solid interaction in axial fan airfoils is one of the main sources of noise, and much research has been conducted to investigate the mechanism of this type of noise. Typical vortex-solid disturbances occur in the column-wing model, and Jacob et al. (2005) experimentally studied the structural and acoustic properties of a tandem rod-airfoil flow field, demonstrating that during vortex-solid interaction, noise mainly comes from aerodynamic interaction at the leading edge of the downstream airfoil. Li et al. (2014) utilized a microphone array to localize noise position and analyzed the far-field acoustic characteristics for different rod-airfoil combinations, at a cross-flow location where the upstream shedding vortex is completely deflected from the leading edge of the airfoil. In this case, the noise of the cylinder-wing model is mainly cylinder-produced noise. In our paper, the airfoil model was tested, and although there is some similarity, e.g., the behavior of the upstream shedding vortex and the vortex-solid interaction, the airfoil noise has its own characteristics.

Much fundamental research has been conducted on the aerodynamic characteristics of the tandem airfoils. Selerowicz et al. (1998) studied the effect of flow separation distance on vortex-solid interaction noise when upstream vortices affect downstream airfoils. Scharpf & Mueller (1992) experimentally investigated the airfoil lift/drag characteristics of two tandem airfoils at

NOMENCLATURE

α_1	upstream airfoil attack angle	U_∞	wind speed, m/s
α_2	downstream airfoil attack angle	*PSD*	power spectra density, dB
c	airfoil chord length, mm	f	frequency, Hz
d	streamwise separation distance between two airfoils	*OASPL*	overall sound pressure level
H	vertical distance between two airfoils	θ	polar angle of far-field microphone against flow direction, deg
S_x	distance between two airfoil geometric centers in x-direction	*POD*	proper orthogonal decomposition
Re_c	Reynolds number ($U_\infty c/v$) based on airfoil chordlength c		

different airfoil difference angles and staggering distances. They pointed out that a combination of two airfoils may outperform a single airfoil in certain flow configurations. Liu (2018) found that the aerodynamic characteristics of both airfoils in tandem are close to optimum when the angle of attack of both airfoils is 10°. To decrease the noise generated by vortex-solid disturbances in the tandem-airfoil model, various approaches have been employed to conduct research on control strategies. Vemuri et al. (2017, 2020) studied the mechanism of sawtooth control of vortex-solid interaction noise under different flow configurations using the sawtooth leading edge of the downstream airfoil. By leveraging blowing at the trailing edge of the upstream airfoil of the tandem airfoil, Winkler et al. (2010) investigated the effect on the aerodynamic characteristics and interaction noise of the tandem airfoil at different blowing rates. Yang et al. (2021) studied the performance of different series of airfoil shapes and investigated numerically longitudinal axis wind turbines with different thicknesses and different airfoil cams. Arcondoulis et al. (2012) studied the mechanism of pitch noise generation for airfoil shapes at zero angles of attack at low and medium Reynolds numbers.

Existing research has indicated that interaction noise between the rotor blades and the static sub is one of the main sources of noise in axial fans, and its noise mechanism and control techniques have been extensively through the study of simplified models such as the tandem rod-airfoil. However, fan rotors and stators are airfoil-shaped and have a certain installation angle (angle of attack) with the direction of flow. The relative variation in attack angle and the relationship between the rotor-stator flow field configuration will affect the total noise of the axial fan. This study investigates the mechanism of noise generation from tandem airfoils at different angles of attack. By adjusting the angle of attack of both airfoils, the noise can be optimized. The findings of this study will assist engineers in designing low-noise axial fans for aerospace and industrial applications.

2. EXPERIMENTAL DETAILS

2.1 Airfoil-Airfoil Tandem Model

The reference model used in this paper is the airfoil in tandem, and its two-dimensional schematic is shown in Fig.1. The airfoil is of type NACA6412 with a chord length of C=100 mm and a spanwise extension of 400 mm. The origin (O) of the Cartesian coordinates (x, y, z) is at the center of rotation of the upstream airfoil, and its specific position is on the line between the leading edge point and trailing edge point of this airfoil, i.e., 30 mm from the leading edge point. The angle of attack (α_1 for the upstream airfoil and α_2 for the downstream airfoil) is defined as the angle between the flow direction and the airfoil chord line, and it is set to 0°, 5°, 10°, 15°, and 20° for each airfoil. Both angles are adjusted by rotating the airfoil against the center of rotation. H and S_x are the vertical distance and the streamwise distance between the center of rotation of two airfoils, respectively. In our experiments, the focus is the parameter study of the attack angle, so H and S_x are fixed at 50 mm and 150 mm, respectively. d is defined as the separation distance between the upstream airfoil trailing edge (TL) and the downstream airfoil leading edge (LE), and it slightly varies as the attack angle changes in the range of approximately 50 mm to 67.2 mm. The flow field between the upstream airfoil wake and the LE of the downstream airfoil is the interested region where the vortex-body interaction phenomenon occurs, which leads to a strong far-field noise. Figure 2 shows the 3D printed model of the tandem airfoil used for the sound field and flow field experiments.

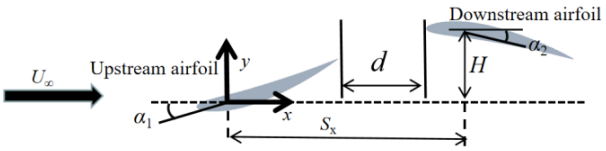

Fig. 1 Two-dimensional schematic of the experimental model and placement

Fig. 2 Physical diagram of the experimental study object

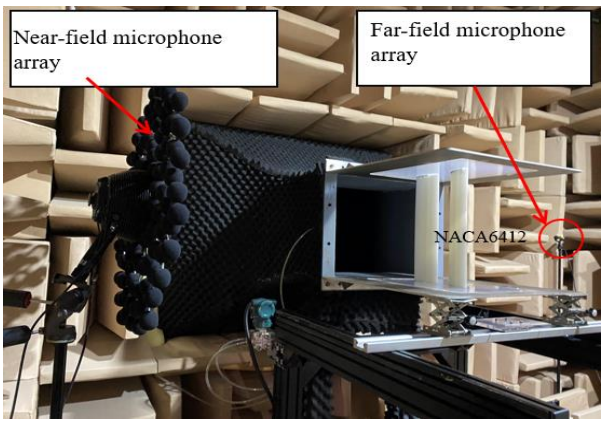

Fig. 3 Test model installation and microphone arrangement in the wind tunnel

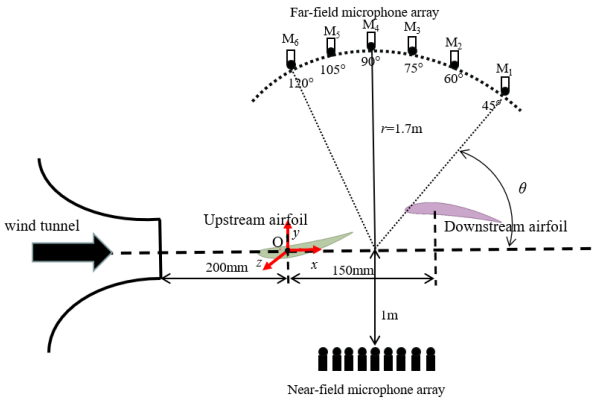

Fig. 4 Two-dimensional diagram of the experimental model and the placement of the measuring equipment

2.2 Experimental Setup

The experiments were conducted in an acoustic wind tunnel laboratory at Wenzhou University. The wind tunnel is a direct-current, open-jet suction wind tunnel with a maximum wind speed of 60 m/s, low background noise, and weak turbulence in Li and Niu (2022). The open test section has a dimension of 0.5 m (width) × 0.4 m (height) × 1.4 m (length). The six walls of the anechoic chamber are fitted with 0.6 m long sound-absorption wedges, and the available space is 4.0 m (length) × 3.3 m (width) × 2.5 m (height), rendering a cut-off frequency of 140 Hz.

The arrangement and test setup of the model and the noise measuring equipment are illustrated in Fig. 3 and Fig. 4. The two airfoils NACA6412 are placed between two endplates that are attached to the nozzle exit. The airfoils can be assumed to be located in the potential core of the jet. A near-field microphone array and a far-field microphone array stand on either side of the test model. The x-axis is parallel to the direction of the incoming flow, the y-axis is perpendicular to the incoming flow, and the z-axis is perpendicular to the x-axis and y-axis. The streamwise distance of the origin (O) from the nozzle exit is 200 mm. The far-field microphone array consists of six microphones (type: BSWA MPA201) numbered M_1-M_6 and arranged at a distance of 1.7 m from the model. The polar angles (θ) of the far-field microphones relative to the flow direction range from 45° to 120°. The microphone M_4 is used mainly for noise comparison as it is perpendicular to the x-streamwise direction. The near-field microphone array is positioned 1 m from the x-z plane of the tandem airfoils, and it consists of 112 MEMS microphones, as demonstrated by Niu et al. (2022) to accurately locate the noise sources. The noise directivity is measured by using the six far-field microphones. For simplicity, no correction is applied to the radiation angle to consider the effect of sound convection and shear layer refraction, and when performing near-field microphone calibration, the camera position is aligned to the center of the model so that the imaging is in the middle position.

Figure 5 presents the particle imaging velocimetry (PIV) test setup for flow field measurements. The laser utilized in this study is a double-pulse type known as the New Wave Gemini Neodymium-Doped Yttrium Aluminum Garnet (Nd:YAG) laser, with a maximum energy output of 120 mJ. The laser sheet thickness in the model area is approximately 1 mm. Images were captured using a Nikon charge-coupled device camera with a resolution of 2456 × 2672 pixels. and more relevant presentations can be found in Niu et al. (2022). The camera was placed directly above the model, and a laser was placed on the side of the model. The laser focused on the middle of the airfoil, i.e., in the z = 0 plane, and the images taken by the camera show the flow around the airfoil in x-y. The main purpose of the flow field

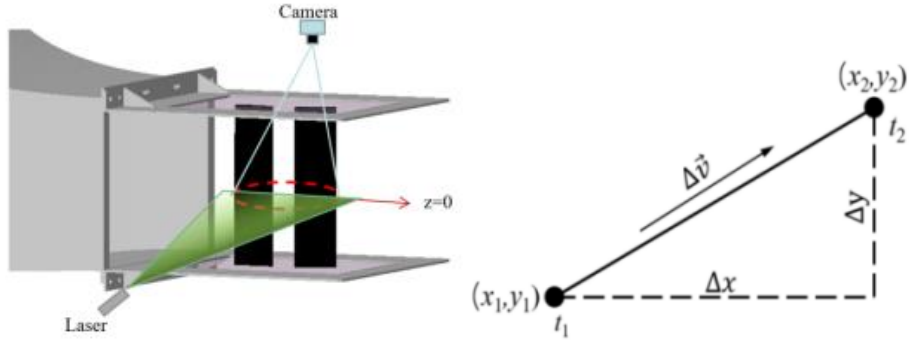

(a) (b)

Fig. 5 Schematic diagram of PIV experimental setup (a) and PIV principle (b)

experiment is to show the flow structure between and around the two airfoils. However, due to the vertical distance difference H between the two airfoils, when the vertical head of the camera is pointed at the downstream airfoil, the image taken will demonstrate the upstream airfoil purely in terms of angular and positional differences.

In this paper, the wind speed ranges from 30 m/s to 50m/s, and the Reynolds number Re_c corresponding to the chord length of the airfoil ranges between 2.2×10^5 and 3.5×10^5.

2.3 Data Acquisition and Processing

The far-field microphone, model BSWA MPA201, was connected to a preamplifier providing power, and a data acquisition card, model NI-USB 6529, was utilized to obtain acoustic data at a sampling frequency of 51,200 Hz. The obtained data was analyzed in 4096 blocks to acquire a frequency resolution of 12.5 Hz, and the PSD was calculated using Welch's method with a Hanning window and a block overlap of 50%. A total of 100 blocks were averaged for statistical confidence. For analysis, the time-domain signal of the acquired sound pressure was processed in Matlab using the p-welch function. When processing the time-domain signal, a Hanning window function was used for each data block to reduce spectral leakage, and 100 data blocks were averaged to obtain statistical confidence.

The acoustic signals from the near-field microphone array were recorded at a sampling rate of 48 kHz for 8s, and the signals were analyzed using a block size of 2048, yielding a frequency resolution of about 24 Hz. Then, the acquired data were post-processed using the eigenvalue-optimized beamforming algorithm to locate the noise sources.

During the PIV experiments, the particles used for the flow were tracer particles produced by burning sulfur and sawdust with an average diameter of about 1 μm. Meanwhile, the thickness of the laser light sheet in the model area was about 1 mm. 500 images of the flow field were acquired at each angle of attack state. Each set of images was processed using a cross-correlation area of 32×32 pixels and an overlay of 50×50%. Based on the captured scale image, the image magnification of the analyzed section was first determined in MicroVec software, then the analyzed section was divided into smaller interrogation (32×32) domains, and the particle images in each interrogation domain were analyzed using a mutual correlation algorithm. The principle of particle image analysis is demonstrated in Fig. 5(b), where x_1 and y_1 are the positions of the particle in image 1, and x_2 and y_2 are the positions of the particle in image 2. Then, the velocity vector field (Δv) is determined from the time interval between the two pulses of the laser generator (Δt). The 500 experimentally recorded pairs of particle images were subjected to correlation calculations, and the results of each pair of images were checked individually, with the original particle images being removed pair by pair if there were large areas of bad spots. Subsequently, all the particle image pairs with good results were subjected to batch calculations to obtain the average velocity vector field of the measured cross-section. Finally, the results of the batch calculation were imported into Tecplot software for further analysis to obtain additional information on the flow field of the photographed section.

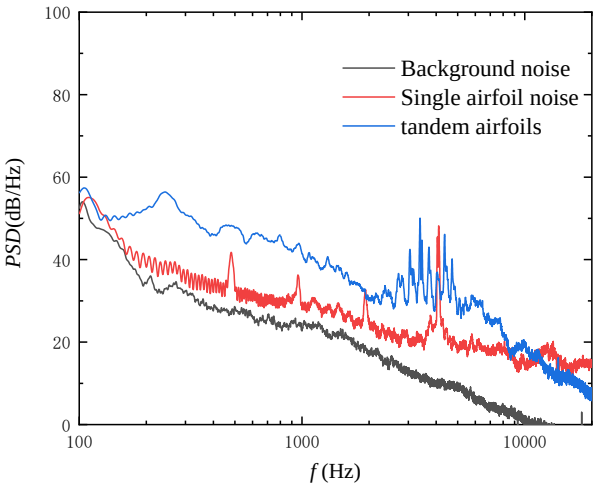

Fig. 6 Background noise and monoplane noise spectrogram

3. RESULTS AND DISCUSSION

3.1 Noise Characteristics at Zero Angle of Attack

Figure 6 shows the background noise and the noise power spectral density (PSD) under a single airfoil in the wind tunnel, as well as the PSD plots of the tandem airfoil at $\alpha_1=\alpha_2=0°$, both measured at $U_\infty=40$ m/s. It can be observed that the background noise of the wind tunnel is mainly broadband noise with a decreasing trend. In contrast, the single airfoil noise spectrogram shows harmonics. When another airfoil is added in front of a single airfoil, the harmonic spike disappears, the entire noise spectrum increases greatly, and a more pronounced tone noise appears between the frequency of 2500-5000 Hz. Humans can generally hear those uncomfortable noises, which are mainly tonal noises caused by these spikes.

Figure 6 demonstrates that when the object of study is a tandem airfoil model, its PSD plot increases significantly compared to the background noise. Meanwhile, the noise spectrum and the total sound pressure level of the tandem airfoil model increase compared to the single airfoil. Additionally, the harmonic peaks in the noise spectrum disappear, while there is tonal noise in the case of $\alpha_1=\alpha_2=0°$.

Before considering the effect of vortex-solid interaction on the noise characteristics of the tandem airfoil at different attack angles, this study first investigates the noise characteristics of the baseline model of the tandem airfoil in parallel, i.e., at a zero angle of attack. Figure 7 shows the measured noise PSD at H=50 mm and three different wind speeds of $U_\infty=30$ m/s, 40 m/s, and 50 m/s with zero airfoil angles of attack ($\alpha_1=\alpha_2=0°$). Distinct humps appear at low frequencies, which are most likely caused by the interaction of the incoming large-

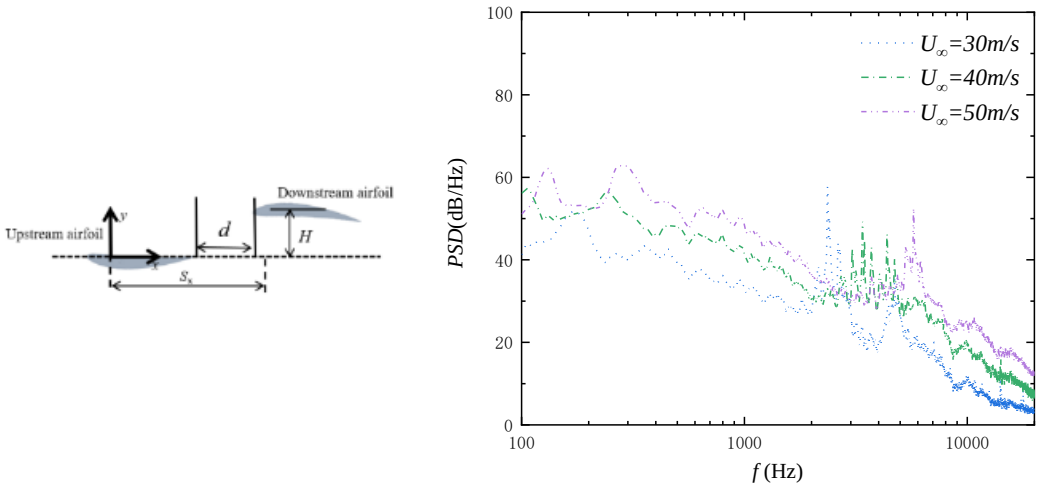

Fig. 7 PSD at U_∞=30 m/s, 40 m/s, and 50 m/s with $\alpha_1=\alpha_2=0°$

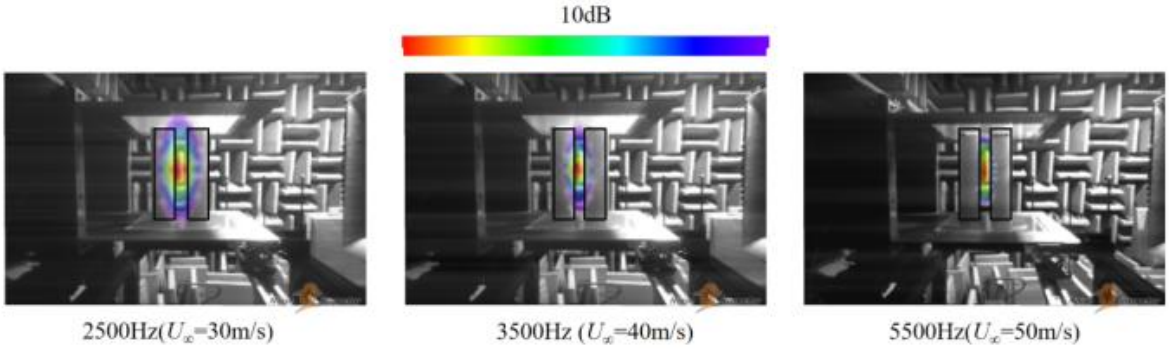

Fig. 8 Sound source location of tonal noise at 30 m/s, 40 m/s, and 50 m/s for the corresponding central frequencies

scale turbulent wake with the leading edges of both airfoils, similar to the turbulence interaction noise identified by Gruber (2012). Within the frequency range of 2 kHz and 5 kHz, there are pronounced spike clusters for all the cases of incoming flow, and the frequency at which the peaks appear increases with the wind speed. The central peak frequencies for wind speeds of 30 m/s, 40 m/s, and 50 m/s are 2500 Hz, 3500 Hz, and 5500 Hz, respectively.

Figure 8 presents the corresponding noise source maps generated by the near-field microphone array for three frequencies. All source locations are at the trailing edge of the upstream airfoil, suggesting that the source of the tone noise is mainly affected by the wake of the upstream airfoil when $\alpha_1=0°$. Since the Reynolds number ranges between 2.2×10^5 and 3.5×10^5, which is in the range of low-mid Reynolds number, the boundary layer of the upstream airfoil is most likely laminar flow. The discrete "ladder-like" tonal noise is caused by the significant increase of T-S (Tollmien-Schlichting) waves in the laminar separation bubble, which turns into K-H instabilities (onset of separation) near the trailing edge. This result has been widely observed by Fink (1975), McAlpine, et al. (1999) and Yakhina et al. (2020) investigating airfoil tonal noise at low/mid Reynolds numbers (1975,1999,2020). Due to the interaction of the upstream turbulence wake, the downstream airfoil may have turbulence boundary layers on both suction and pressure sides, with no tonal noise at its trailing edge. As the vertical separation H further increases, it can be expected that tonal noise will appear on the trailing edges of both airfoils at a certain distance.

3.2 Noise Characteristics at Different Angles of Attack

The changes in the attack angles will change the wake interaction and noise characteristics. Figures 9 shows the noise spectrum of the tandem airfoil at the fixed angles of $\alpha_1=20°$ and $\alpha_2=10°$ for H=50 mm and U_∞=30 m/s, 40 m/s, and 50 m/s, respectively. Compared to the spectrum at $\alpha_1=\alpha_2=0°$ in Fig. 6, the obvious difference is that the noise is broadband without any discrete tonal peaks, suggesting that the turbulent boundary layer or wake, not the laminar flow, dominates the flow characteristics. The noise source map for the frequency of 3150 Hz in Fig.10 shows that the dominant noise source is located at the leading edge of the downstream airfoil where the turbulence wake of the upstream airfoil impinges. For different wind speeds, except for an increase in the magnitude of the sound pressure level, the spectrum curve trend and the location of the sound source remain the same. Thus, the following investigations will focus on the wind speed U_∞=40 m/s.

Then, this study investigates the noise characteristics with various angles of attack α_1 and a fixed α_2. Figure 11

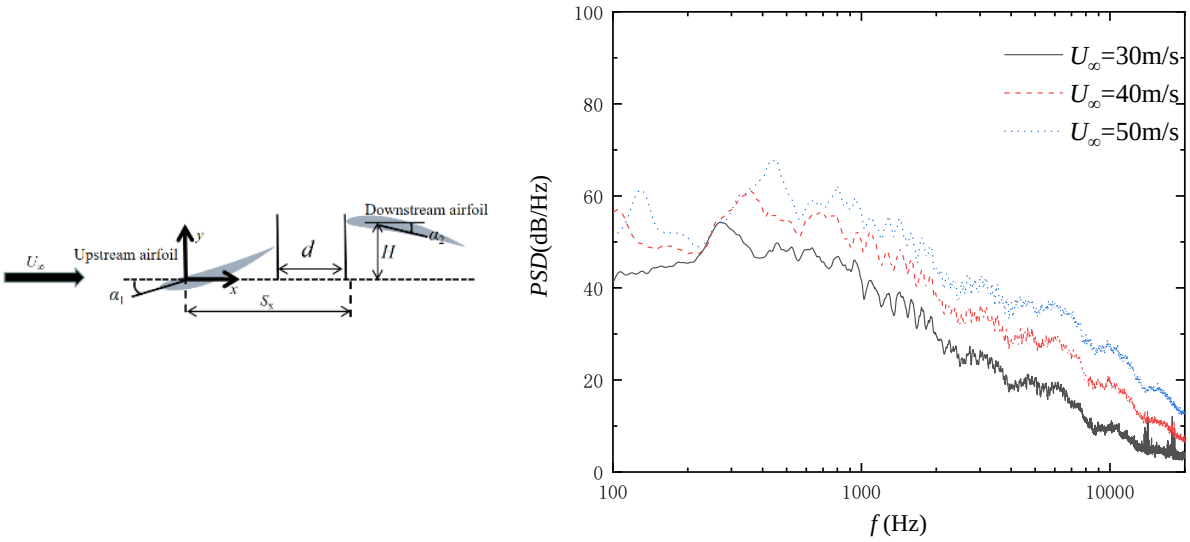

Fig. 9 PSD at U_∞=30 m/s, 40 m/s, and 50 m/s with α_1 = 20° and α_2 = 10°

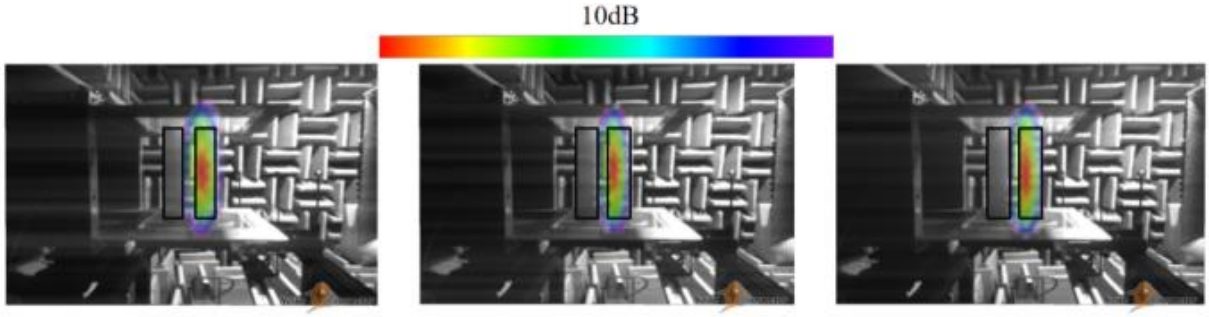

Fig. 10 Sound source location of tonal noise at 30m/s, 40m/s, and 50m/s for the frequency of 3150 Hz

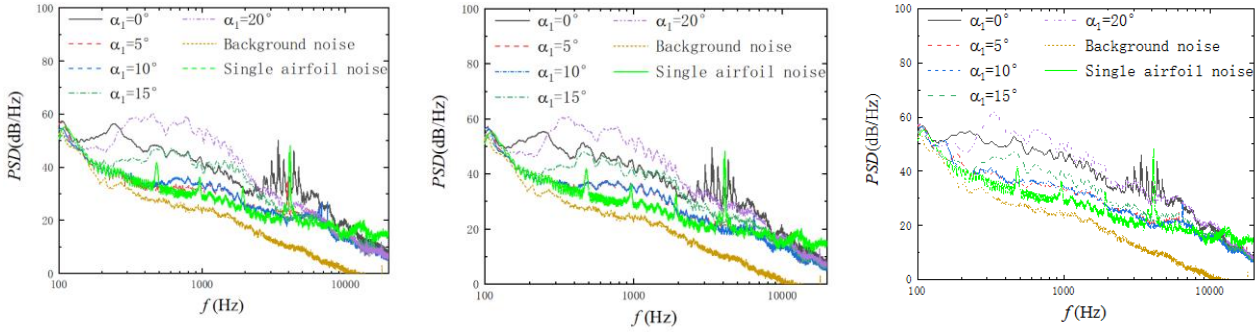

a (α_2=0°) b (α_2=5°) c (α_2=10°)

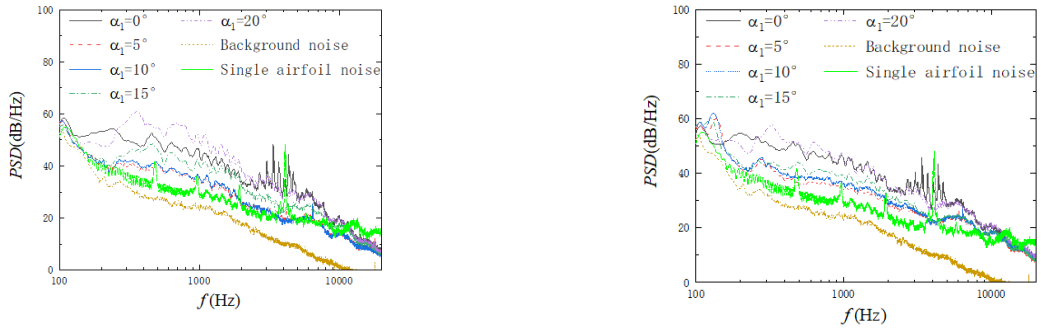

d (α_2=15°) e (α_2=20°)

Fig. 11 Far-field noise spectrum measured by fixing the angle of attack α_2 and adjusting α_1

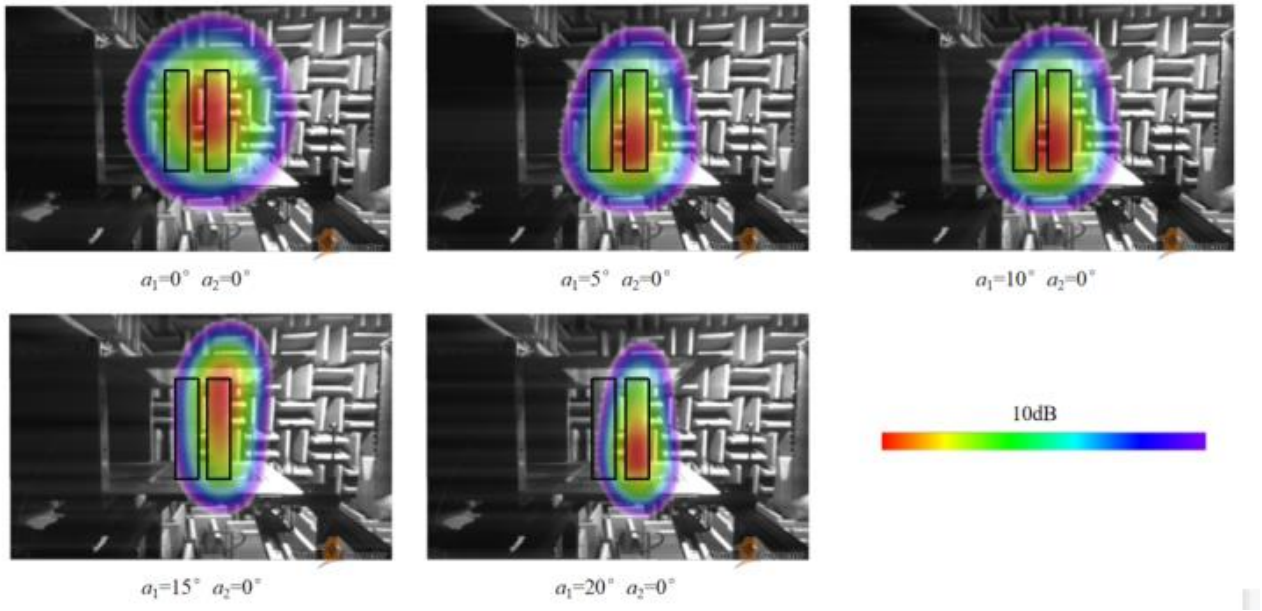

Fig. 12 Near-field noise localization measured by fixing the angle of attack α_2 = 0° and adjusting α_1(0°, 5°, 10°, 15°, and 20°)

(a-e) illustrates the measured PSD for different α_1 at each α_2 = 0°, 5°, 10°, 15°, and 20°, respectively. At α_1=0°, the noise spectrum shows a ladder-like discrete form between 2500 and 5000 Hz for all cases of α_2 and the black lines shown in each figure. The noise characteristic is consistent with the trailing edge tonal noise of an airfoil laminar boundary layer at low-mid Reynolds numbers. Nevertheless, as the upstream airfoil angle α_1 increases, the noise spectrum changes dramatically. At α_1=5°, the ladder-like discrete tones disappear, and there is only one single peak noise for α_2=0°, and none for other angles α_2. Additionally, the noise reaches its lowest level and, in the frequency range of 200 to 8000 Hz, is 10 dB less compared to that at α_1=0°. At α_1=10°, the noise spectrum has the same broadband characteristics and levels as that at α_1=5°. Further increasing the angle α_1 to 15° and 20°, the broadband noise increases greatly compared to α_1=5°.

Regarding the variation of the broadband noise source, Fig. 12 shows the noise source positioning diagram for the frequency of 1250 Hz with the variation of angle α_1 (α_2=0°). It can be seen that as the angle of attack α_1 increases, the position of the noise source gradually moves from the position of the leading edge of the downstream airfoil to the surface of the downstream airfoil. Figure 13 presents a graph of the variation of overall sound pressure level (OASPL) with angle. Here, the OASPL is obtained by integrating the PSD in the frequency range between 140 Hz (the cut-off frequency of the anechoic chamber) and 10 kHz. When α_2=0°, as α_1 increases from 0° to 10°, the maximum value of noise is significantly reduced; when continuing to increase α_1 to 20°, it is found that the OASPL also increases, indicating that adjusting α_1 within a certain range can reduce the noise, and once the range is exceeded, the noise will increase. Adjusting α_1 when α_2 is at any angle leads to a similar observation that the noise falls within a certain range and rises beyond that. As illustrated in Fig. 11, when

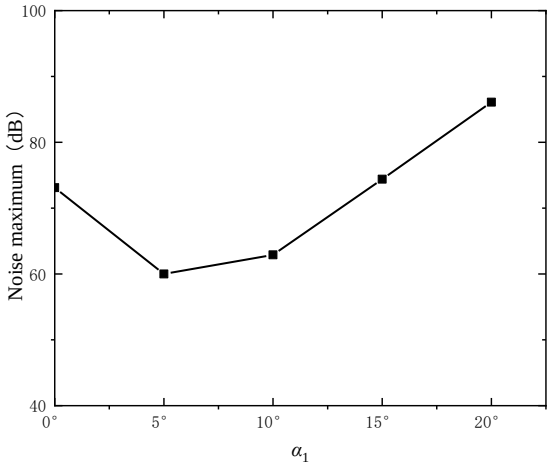

Fig. 13 Variation of the OASPL with α_1

α_2 is at any angle, compared with the case of α_1=0°, if α_1<10°, the noise is significantly reduced, and when α_1>15°, the noise spectrum gradually increases, indicating that the interaction between the upstream wing wake and the downstream wing is not obvious when α_1<10°, while the interaction is significantly strengthened when α_1>15°, and the noise source is also mainly generated by the interaction between the upstream wing wake and the downstream wing.

Figure 14(a-b) shows the measured PSD versus the frequency after adjusting α_2 for different fixed α_1 angles (0 and 15°). When the angle of attack α_1 is adjusted from 0 to 15°, the tone noise generated disappears slowly, and the broadband noise becomes the main source of the noise. By adjusting the two airfoils separately, the noise generation mechanism changes, and the main location of the source is not fixed at the trailing edge of the upstream airfoil.

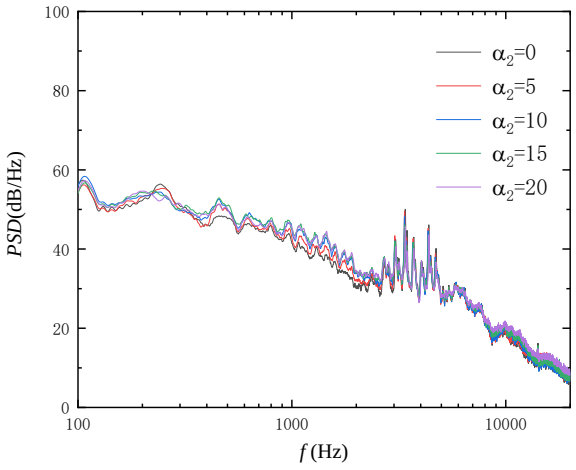

a (α_1=0°)

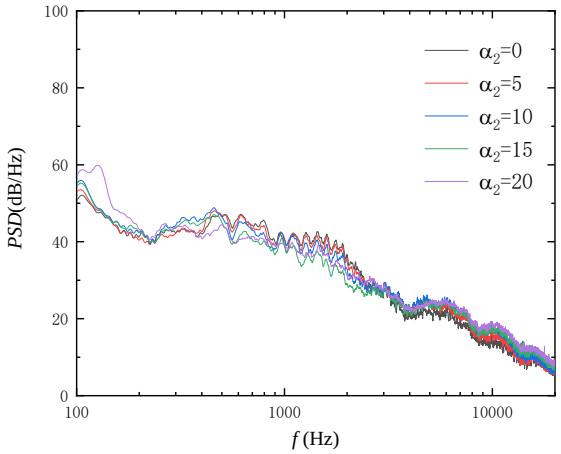

b (α_1=15°)

Fig. 14 Far-field noise spectrum measured by fixingα_1 and adjusting α_2

Figure 15 displays the sound source localization achieved by adjusting α_1 while maintaining a fixed α_2 at the frequency of 3150 Hz. When comparing this with Fig. 10 (where α_2 is 0), it is evident that at a 0° angle of attack (α_1), there is minimal interaction between the wake generated by the upstream airfoil and the downstream airfoil. The tonal noise in Fig. 11 (at α_2=0) is due to the pressure pulsations at the trailing edge of the upstream airfoil. When α_1 is increased to 20°, the noise source gradually shifts from the trailing edge of the upstream airfoil to the leading edge of the downstream airfoil, indicating the onset of interaction between the wakes of the two airfoils. Under the condition of α_2=0°, the area of interaction between the trailing airflow of the upstream airfoil and the downstream airfoil is limited, and most of the airflow collides with the leading edge of the downstream airfoil. This leads to the gradual disappearance of the tonal noise as interaction occurs and the emergence of broadband noise. These findings indicate that the presence and disappearance of tonal noise are intricately related to the angle of attack of the airfoil, highlighting the effect of changes in the angle of attack of the upstream airfoil.

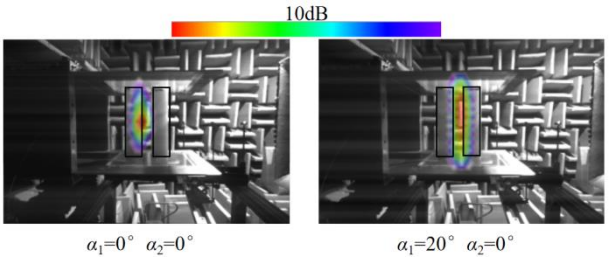

Fig. 15 Measured sound source localization after fixing α_2 = 0° and adjusting α_1 (3150Hz)

When the angle of attack α_1 is 0°, as shown in the first graph of Fig. 16 at the frequency of 3150 Hz, the noise originating from pressure pulsations at the trailing edge mainly manifests as tonal noise. Further analysis in conjunction with Fig. 17 demonstrates that at low and medium Reynolds numbers (Re_c=2.9×10^5), the predominant source of tonal noise aligns with the position of the trailing edge of the upstream airfoil. This characteristic remains consistent even after α_2 is adjusted, indicating the substantial influence of the upstream airfoil on tonal noise generation. At specific frequencies, tonal noise usually exhibits an intensity about 10 dB higher than broadband noise, making it a more noticeable and

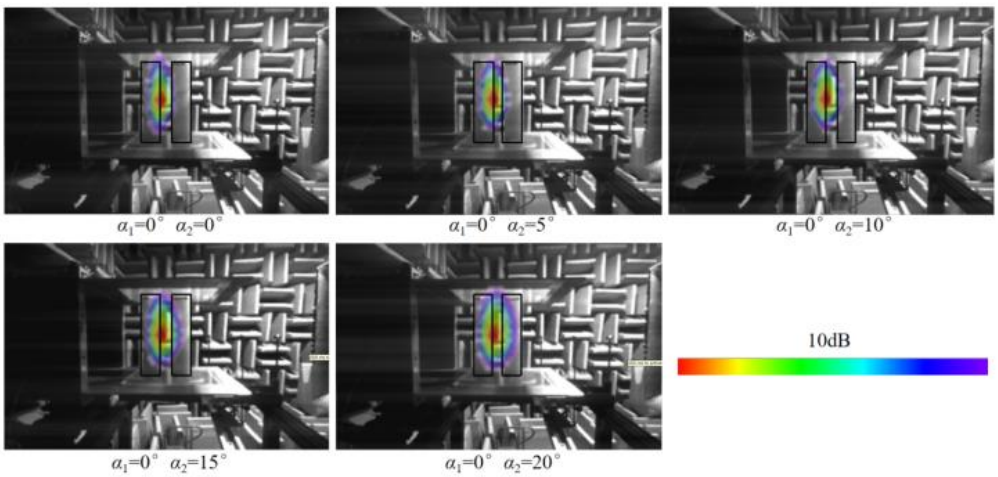

Fig. 16 Near-field source localization was measured by fixing the angle of attack α_1= 0° and adjusting α_2

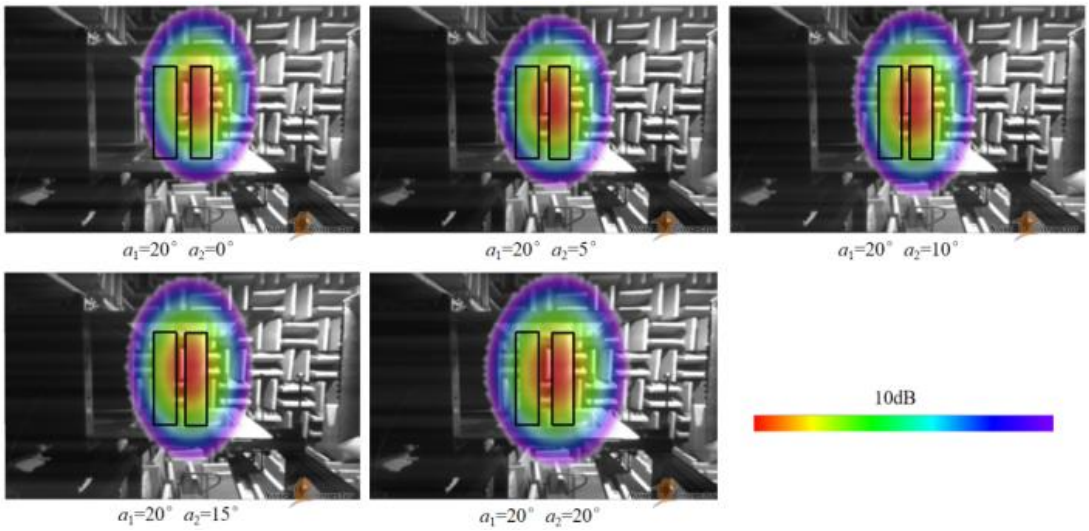

Fig. 17 Near-field source localization measured by fixing α_1=20° and adjusting α_2

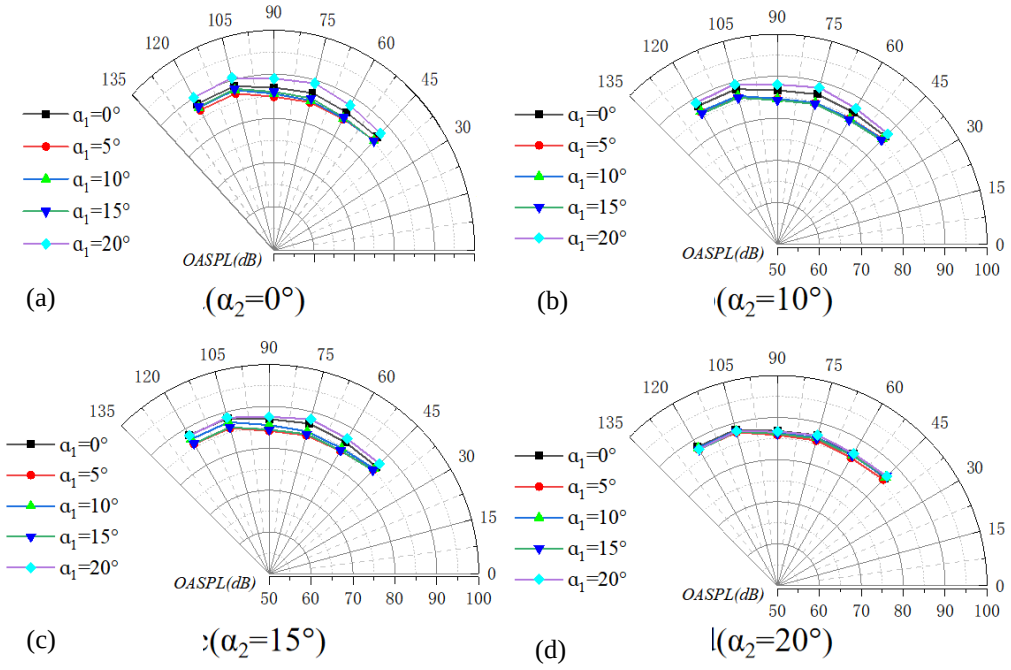

Fig. 18 Noise directivity of the airfoil OASPL with different α_2 (0, 10, 15, and 20) measured by 6 microphones

Table 1 Overall sound pressure levels measured in the experiment

	α_1=0°	α_1=5°	α_1=10°	α_1=15°	α_1=20°
α_2=0°	87.0	84.9	85.6	86.0	89.0
α_2=5°	86.7	84.5	85.3	85.0	88.2
α_2=10°	86.7	84.6	84.7	84.3	88.0
α_2=15°	86.9	84.2	85.5	84.4	87.5
α_2=20°	86.8	85.9	86.4	86.1	86.7

potentially bothersome acoustic feature. In the context of Fig. 17, for α_1=20°, the adjustment of α_2 leads to a notable shift in the sound source location from the trailing edge to the leading edge of the downstream airfoil. This shift signifies the interaction between the trailing airflow of the upstream airfoil and the downstream airfoil, resulting in a transition from tonal noise to broadband noise.

Table 1 shows the OASPL measured in the experiment, all the data listed are measured by the M_4 (θ=90) far-field microphone. From this table, it can be seen that at α_1=5° and α_2=15°, OASPL is the smallest; while at α_1=20° and α_2=0°, the total sound pressure level reaches the maximum level. The change in OASPL is relatively large when adjusting α_1, and it is not obvious when adjusting α_2, suggesting that the change in α_1 in a tandem airfoil has a greater impact on the overall noise level than that in the downstream airfoil. This can be seen in conjunction with Fig. 18, where the noise levels

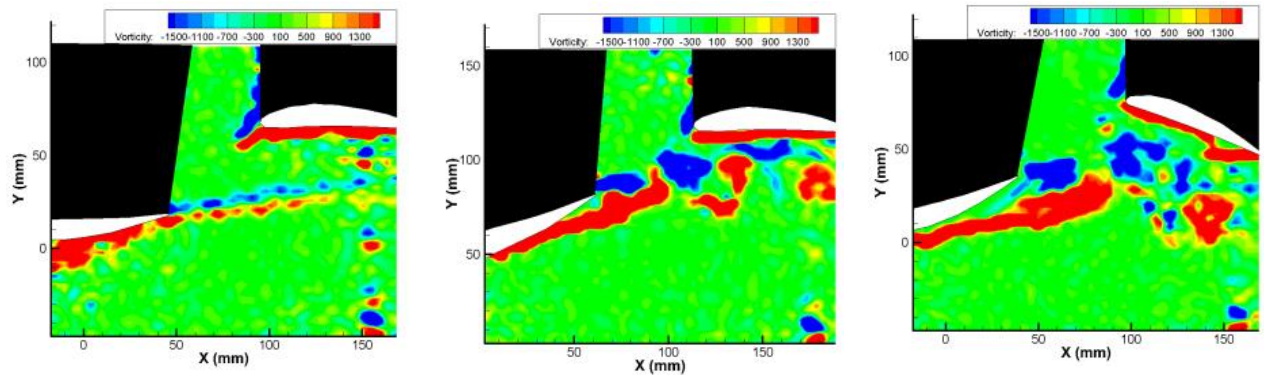

(a) (b) (c)

Fig. 19 Instantaneous vortex cloud at a wind speed of 40 m/s with both α_1 and α_2 at 0 (a); α_1 at 15 and α_2 at 0 (b); α_1 at 15° and α_2 at 20° (c)

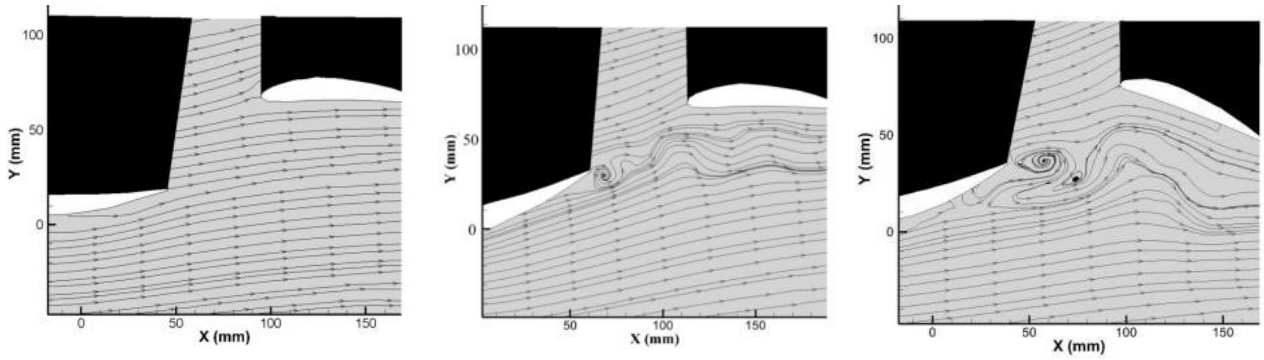

(a) (b) (c)

Fig. 20 Flow line diagram at a wind speed of 40 m/s at 0° for both α_1 and α_2 (a); α_1 at 15° and α_2 at 0° (b); α_1 at 15° and α_2 at 20° (c)

obtained at M_5 (θ=105°) are significantly higher than the other noise levels. It suggests that the noise source is closer to M_5, which also indicates that the main sound source location is near the upstream airfoil.

3.3 PIV Experimental Measurement

Figure 19 shows the plots of the flow field measured by the PIV. Specifically, Fig. 19(a) shows the measured instantaneous vortex clouds at α_1=0° and α_2=0°, Fig. 19(b) shows the measured vortex clouds at α_1=15° and α_2=0° and Fig. 19(c) shows the measured vortex clouds at α_1=15° and α_2=20°. It can be seen from Fig. 19 that when α_1 and α_2 are both 0°, there is little interaction between the upstream and downstream airfoils. As α_1 increases, the shedding vortex at the trailing edge of the upstream and the downstream airfoils exhibit obvious interacting effects, i.e., the shedding vortex of the upstream airfoil hits the downstream airfoil, and the interaction between the two airfoils is increasingly obvious. This can be also observed in Fig. 20. In Fig. 20 (b) and (c), the vortex volume increases significantly, and a more pronounced vortex appears behind the upstream airfoil. This is due to the increase in the windward angle of attack of the upstream airfoil. It causes an increase in its windward area and the pressure difference between the windward and leeward sides of the upstream airfoil, which in turn leads to a larger vortex cloud.

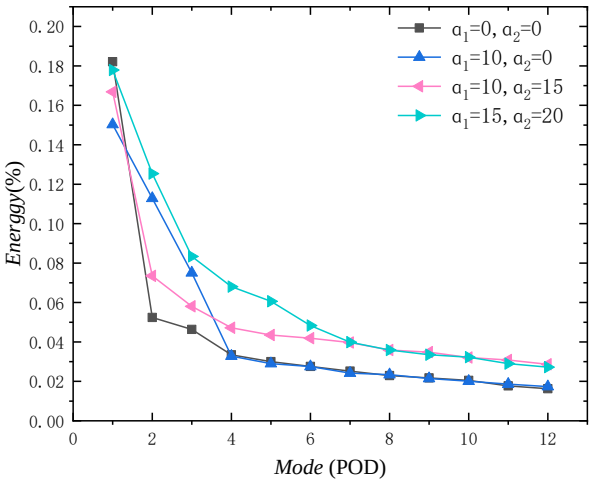

Fig. 21 Percentage of energy accounted by the POD mode for the four different angles of attack for the tandem airfoils

Figure 21 shows the percentage of energy accounted for by the first 12 proper orthogonal decomposition (POD) modes for the tandem airfoil at the four different angles of attack. The main mode (mode-1) accounts for 18.22%, 17.9%, 16.34%, and 15.03% of the energy of the four

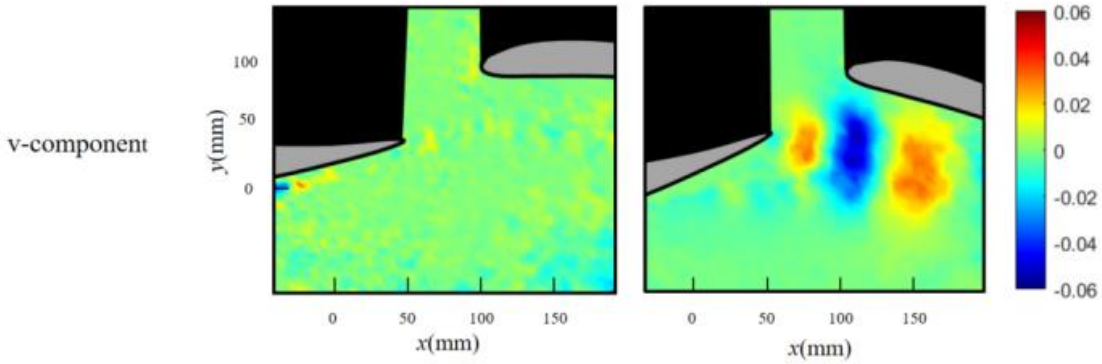

Fig. 22 Comparison of POD mode 1 at two angles of attack

angles of attack, respectively, indicating that the dominant noise source is the large-scale vortex shedding. When α_1 is not equal to 0°, the percentage of the energy of each POD mode between mode-2 and mode-12 is higher than that when α_1=0°. This suggests that the non-constant pulsations move towards the higher-order harmonic spatial structure, which explains the increase in the far-field broadband noise in the high-frequency region when α_1 is greater than 0°. This phenomenon is consistent with the result in Fig. 13, where the noise throughout the model is mainly broadband noise.

Figure 22 shows the variation of mode 1 for α_1=α_2=0° and α_1=15° and α_2 =20°. This figure demonstrates that when α_1=0°, no significant energy component appears at its trailing edge, and when α_1 is 15°, a significant energy component appears at its trailing edge. Combined with the vortex cloud in Fig. 19, it can be seen that as α_1 increases, a significant vortex-shedding structure appears at its trailing edge.

4. CONCLUSION

This paper experimentally investigates the noise generation mechanism of a tandem airfoil with various angles of attack. By adjusting the angle of attack of both airfoils, the noise can be optimized. The main conclusions are as follows:

1) When the vertical distance between two airfoils H=50 mm, for the same state of the airfoils, increasing the incoming wind speed will not change the noise generation mechanism but the sound pressure magnitude and the frequency of noise occurrence. Meanwhile, when the angle of attack is adjusted, the noise source will change. When the attack angle α_1 of the upstream airfoil is small (α_1<15°), its wake hardly interacts with the downstream airfoil, and the noise source is mainly concentrated at the trailing edge of the upstream airfoil. When the angle of attack α_1 is larger than 15°, the upstream wake interacts with the downstream airfoil, and the noise radiates from the lead edge.

2) When α_1=0°, no matter how α_2 is adjusted, the tone noise will eventually appear. The discrete “ladder-like” tonal noise is radiated by the scattering of the increased pressure pulsation (T-S) at the trailing edge. By using the near-field noise location array technique, it is found that the sound source at the corresponding frequency is mainly concentrated at the trailing edge of the upstream airfoil. The tone noise gradually disappears when α_1 is increased, and the broadband noise becomes the main noise. Also, the location of the sound source gradually transitions from the upstream airfoil to the downstream airfoil. The comparison of the OASPL and the sound directivity diagram indicates that the noise is mainly affected by the upstream airfoil, and noise sources are mainly concentrated in the upstream airfoil.

3) After analyzing the PIV technique and the POD modal, it can be concluded that when α_1=0°, there is no obvious vortex shedding or energy clouds at the trailing edge of the upstream airfoil. However, as α_1 increases, more distinct vortex shedding can be observed at the trailing edge of the upstream airfoil, leading to a noticeable vortex-solid interaction with the downstream airfoil. This directly illustrates the mechanism of noise generation and indirectly illustrates the variation of noise with the angle of attack.

In the tandem airfoil, changing the state of the airfoil has a large impact on the noise generation mechanism. From this perspective, further study needs to be conducted on noise control. Meanwhile, small holes and fairings can be used to interact with the airfoil generation mechanism, thus achieving noise reduction.

ACKNOWLEDGEMENTS

The experiments are made possible through the joint supports provided by the National Natural Science Foundation of China (Grant No: 11972022) and the Key Laboratory for Aerodynamic Noise Control (No：ANCL20210202), China Aerodynamic Research & Development Centre, which are gratefully acknowledged.

CONFLICT OF INTEREST

No potential conflict of interest was reported by the authors.

AUTHORS CONTRIBUTION

Weijie Shi: Conceptualization, Software, Validation, Visualization, Writing - Original Draft, Investigation.

Yong Li: Software, Formal analysis, Visualization, Methodology, Software, Validation, Formal analysis, Visualization. **Jianxi Zhou**: Conceptualization, Methodology, Validation, Formal analysis, Writing - Review & Editing, Funding acquisition. **Zhengwu Chen**: Supervision, Project administration.

REFERENCES

Arcondoulis, E., Doolan, C., Brooks, L., Zander, A. (2012). *On the generation of airfoil tonal noise at zero angle of attack and low to moderate Reynolds number*. 18th AIAA/CEAS Aeroacoustics Conference (33rd AIAA Aeroacoustics Conference), 2060. https://doi.org/10.2514/6.2012-2060

Fink, M. R. (1975). Prediction of airfoil tone frequencies. *Journal of Aircraft*, *12*(2), 118-120. https://doi.org/10.2514/3.44421.

Gruber, M. (2012). Airfoil noise reduction by edge treatments. Diss. University of Southampton. http://eprints.soton.ac.uk/id/eprint/349012

Jacob, M, C., Boudet, J., Casalino, D., & Michard, M. (2005). A rod-airfoil experiment as a benchmark for broadband noise modeling. *Theoretical and Computational Fluid Dynamics*, *19*(3), 171-196. https://doi.org/10.1007/s00162-004-0108-6

Li, Y., & Niu, X. F. (2022). Rod–airfoil interaction noise at different rod cross sections and airfoil angles. *AIAA Journal*, *60*(6), 3635-3650. https://doi.org/10.2514/1.J061303i

Li, Y., Wang, X., Chen, Z., Chen, Z., & Li, Z. (2014). Experimental study of vortex–structure interaction noise radiated from rod–airfoil configurations. *Journal of Fluids and Structures*, *51*, 313-325. https://doi.org/10.1016/j.jfluidstructs.2014.08.014

Liu, X. (2018). *Aerodynamic and wake development of aerofoils with trailing-edge serrations* [Ph.D. thesis, University of Bristol]. https://research-information.bris.ac.uk/ws/portalfiles/portal/181451764/Final_Copy_2018_11_06_Liu_X_PhD.pdf

Longhouse, R. E. (1976). Noise mechanism separation and design considerations for low tip-speed axial-flow fans. *Journal of Sound and Vibration*, *48*(4), 461-474. https://doi.org/10.1016/0022460X(76)90550-2.

McAlpine, A., Nash, E. C., & Lowson, M. V. (1999). On the generation of discrete frequency tones by the flow around an aerofoil. *Journal of Sound and Vibration*, *222*(5), 753-779. https://doi.org/10.1006/JSVI.1998.2085

Niu, X. F., Chen, H. J., Li, Y., Jia, X. Y., Zhang, Y. W., & Yong, X. (2022). Design and performance of a small-scale acoustic wind tunnel at Wenzhou University for aerodynamic noise studies. *Applied Acoustics*, *199*, 109010. https://doi.org/10.1016/j.apacoust.2022.109010.

Scharpf, D. F., & Mueller, T. J. (1992). Experimental study of a low Reynolds number tandem airfoil configuration, *Journal of Aircraft, 29*(2), 231-236. https://doi.org/10.2514/3.46149.

Selerowicz, W., Sobieraj, G., & Szumowski, A. (1998). Effect of miss-distance on the airfoil-vortex interaction. *Experiment. Archives of Mechanics*, *50*(4), 691-701. https://doi.org/10.1109/IDAACS.2005.282979

Vemuri, S., Liu, X., Zang, B., & Azapeyvand, M. (2017). On the application of trailing-edge serrations for noise control from tandem airfoil configuration. *AIAA paper*, *3716*. https://doi.org/10.2514/6.2017-3716

Vemuri, S., Liu, X., Zang, B., & Azapeyvand, M. (2020). On the use of leading-edge serrations for noise control in a tandem airfoil configuration. *Physics of Fluids*, *32*, 077102. https://doi.org/10.1063/5.0012958

Winkler, J., Carolus, T., Scheuerlein, J., Dinkelacker, F. (2010). Trailing-edge blowing on tandem airfoils: Aerodynamic and Aeroacoustic Implications. *16th AIAA/CEAS Aeroacoustics Conference*, *3981*. https://doi.org/10.2514/6.2010-3981

Yakhina, G., Roger, M., Moreau, S., et al. (2020). *Experimental and analytical investigation of the tonal trailing-edge noise radiated by low Reynolds number aerofoils.* Acoustics. MDPI. https://doi.org/10.3390/acoustics2020018.

Yang, Y., Pröbsting, S., Liu, Y., Zhzng, H., & Li, Y. (2021). Effect of dual vortex shedding on airfoil tonal noise generation. *Physics of Fluids*, *33*(7), 075102. https://doi.org/10.1063/5.0050002.